The Balance Between Shear Flow and Extracellular Matrix in Ovarian Cancer-on-Chip

Changchong Chen, Alphonse Boché, Zixu Wang, Elliot Lopez, Juan Peng, Franck Carreiras, Marie-claire Schanne-Klein, Yong Chen, Ambroise Lambert, Carole Aimé

The balance between shear flow and extracellular matrix in ovarian cancer-on-chip

Changchong Chen,[1] Alphonse Boché,[2] Zixu Wang,[1] Elliot Lopez,[1] Juan Peng,[1] Franck Carreiras,[2] Marie-Claire Schanne-Klein,[3] Yong Chen,[1] Ambroise Lambert,[2] Carole Aimé[1*]

[1] PASTEUR, Département de chimie, École normale supérieure, PSL University, Sorbonne Université, CNRS, 75005 Paris, France
[2] Equipe de Recherche sur les Relations Matrice Extracellulaire-Cellules, ERRMECe, (EA1391), Groupe Matrice Extracellulaire et physiopathologie (MECuP), Institut des Matériaux, I-MAT (FD4122), CY Cergy Paris Université, France
[3] Laboratoire d'Optique et Biosciences (LOB), École polytechnique, CNRS, Inserm, Institut Polytechnique de Paris, F-91128 Palaiseau, France

E-mail: carole.aime@ens.psl.eu

Abstract

Ovarian cancer is the most lethal gynecologic cancer in developed countries. In the tumor microenvironment, the extracellular matrix (ECM) and flow shear stress are key players in directing ovarian cancer cells invasion. We use artificial ECM models based only on ECM proteins to build an ovarian tumor-on-chip to decipher the crosstalk between ECM and shear stress on the migratory behavior and cellular heterogeneity of ovarian tumor cells. This work shows that in the shear stress regime of the peritoneal cavity, the ECM plays a major role in driving individual or collective ovarian tumor cells migration. In the presence of basement membrane proteins, migration is more collective that on type I collagen regardless of shear stress. With increasing shear stress, individual cell migration was enhanced, while no significant impact on collective migration was measured. This highlights the central position that ECM and flow shear stress should hold in *in vitro* ovarian cancer models to deepen our understanding of cellular responses, and improve the development of ovarian cancer therapeutic platforms. In this frame, adding flow provides significant improvement in biological relevance over our previous work. Further steps for enhanced clinically relevance require not only multiple cell lines but patient-derived cells and sera.

Keywords: Ovarian Tumor-on-Chip; Migration; Tumor Spheroids; Extracellular Matrix; Flow Shear Stress.

1. Introduction

Ovarian cancer (OC) is the fifth most frequent cause of cancer death in women in developed countries [1]. This is attributed to the lack of visible and reliable symptoms during the onset of the disease, which results in patients being diagnosed at an advanced stage with an increased probability of metastasis to distant organs. The biology of OCs differs from that of hematogenous metastasizing tumors because OC cells primarily disseminate within the peritoneal cavity. Most OCs result from the transformation of ovarian epithelial cells that grow into spheroids at a primary site and spread flowing through the pathological fluid that accumulates in the peritoneal cavity, called ascites [2]. In the course of this metastatic journey, tumor cells in their ascitic peritoneal environment are subjected to a low (less than a $dyn.cm^{-2}$) isotropic shear stress resulting from walking and breathing movements [3]. Epithelial cells eventually undergo the epithelial-to-mesenchymal transition (EMT) and lose their epithelial characteristics for mesenchymal ones. This is associated with the weakening of their interactions with the basement membrane and the loss of cell-to-cell junction proteins like E-cadherin [4,5]. This works as a continuum, generating high cellular heterogeneity with intermediate cell states with varying expression of epithelial and mesenchymal markers. These hybrid states have been associated *in vitro* with improved metastatic properties including migration and invasion and increased cell survival in suspension. This also involves significant remodeling of the extracellular matrix (ECM), and the loss of basement membrane proteins, including collagen IV and laminin [6-8].

Advances in cancer research require the ever improvement of *in vitro* models to reproduce the tumor microenvironment, which is known to impact cell proliferation, migration, invasion, and apoptosis [9]. The ovarian tumor microenvironment mainly includes (i) tridimensional cell constructs - spheroids, (ii) the circulating environment, and (iii) the extracellular matrix (ECM). OC cells are likely to form spheroids, which may contribute to protect them from the circulating microenvironment [10] and to resist chemotherapies [11,12]. Many research efforts have been dedicated to the engineering of spheroid models using various strategies such as cell suspension culture, hanging drop, microwell arrays, or microfluidics

[13-19]. We have recently reported the microfabrication of non-adherent cages whose tunable dimensions enable tuning the spheroid size in a well-controlled and reproducible fashion [20]. In OC, the control over the circulating environment is particularly relevant, because OC cells benefit from the unique liquid microenvironment of the ascites exposing OC cells to flow shear stress. Microfluidic chips have mainly been developed to investigate the impact of shear stress on attachment, growth, and motility of OC cells [21,22], the reorganization of the cytoskeleton under shear stress [23,24], and also the pathways involved in chemoresistance of non-adherent spheroids [25,26]. More recently, setups have been reported including vessels in multicellular constructs providing models to elucidate tumor-stromal cell interactions during intraperitoneal metastasis of OC [27-29]. Care must also be paid to the reconstruction of the surrounding ECM. This most often includes a layer of fibronectin [21], growth factor reduced (GFR) Matrigel [27], and its mixture with collagen I [30,31], denuded amniotic membranes [24], fibrin hydrogels [29] and synthetic polymer coating [25,26].

Following previous works, we have built two ECM models made up of type I collagen, which is by far the major structural element of the ovarian stroma, eventually topped with layers of type IV collagen and laminin [32]. Collagen IV and laminin are two of the most abundant extracellular proteins in the mesothelium, which is extensively remodeled during OC. Collagen IV and laminin have been shown to be transiently lost in pre-malignant ovarian surface epithelium [6-8], which makes it relevant to build models differing in their composition to mimic early and late stages of ovarian cancer. These ECM models exhibit stiffness in the range of the physiological, including pathological tissues, *i.e.* from few to tens of kPa [32]. This is made possible by the use of porous supports that maintain large areas of self-standing tissues, while allowing flow exchanges [33-35], and that can be easily integrated into a microfluidic chip system. Compared with our previous work on the impact of ECM on cancer cell lines, two major improvements should be highlighted here: the use of cancer spheroids rather than isolated cells, and the integration of flow, which represents a key improvement in terms of biological and medical relevance.

By using only ECM proteins and different flow conditions, we aim to develop an ovarian cancer-on-chip and assess the crosstalk between ECM and shear stress in ovarian adenocarcinoma cell response. Our results show that migration - whether individual or collective - strongly depends on the ECM, in the shear stress regime of the peritoneal cavity. Finally, in terms of morphology, the impact of the ECM was lowered under flow, and the shear stress appears to overcome the features of the ECM. These findings show the unique ability of our model to reproduce the ovarian tumor ECM and ascites flow microenvironment to uncouple biochemical and physical cues and analyze their impact on the migratory behavior and morphology of cells.

2. Materials and methods

2.1. Fabrication of the porous supports

Porous supports similar to the ones that are commercially available from the Mesobiotech® company were fabricated by photolithography and soft-lithography in the lab as previously reported (see Supporting Information) [32]. The honeycomb structure we use follows a bioinspired honeycomb approach. This geometry ensures maximum strength of the support structure while minimizing the amount of material and maximizing lightness. The width of the honeycombs was optimized within the range of 200 to 400 µm and finally set at 400 µm, with a frame width of 50 µm and a thickness of 50 µm to guarantee the lowest contribution to the mechanical properties of the support (see Supporting Information, Figure S1).

2.2. ECM fabrication

Type I collagen was extracted and purified from rat tail tendons as previously described, except that we used 3 mM hydrochloric acid instead of 500 mM acetic acid [36,37]. Collagen purity was assessed by electrophoresis and its concentration was estimated by hydroxyproline titration [38]. All other chemicals were purchased and used as received. Water was purified with a Direct-Q system (Millipore Co.). Two ECM models were prepared. The first one is an artificial connective tissue (ACT) from type I collagen

only. A PBS solution at pH 9 was prepared by slowly adding 1M NaOH to 1X PBS (pH = 7.4) to induce collagen I fibrillogenesis from acidic collagen I solution (20 µL with 1 mg/mL in PBS). The second model, called artificial basement membrane (ABM), contains type I collagen (1 mg/mL in PBS), type IV collagen (0.5 mg/mL in PBS, from the human placenta), and laminin (10 µg/mL in deionized (DI) water, from Engelbreth-Holm-Swarm murine sarcoma basement membrane). Each component was drop cast layer by layer in the following order: type I collagen, type IV collagen, and laminin. In each step, 20 µL of the solution was poured on the patch and dried in air at room temperature before the next step of drop casting (Figure 1A). Finally, the ECM was washed with DI water, dry in air at room temperature, and could be stored in the fridge at 4°C.

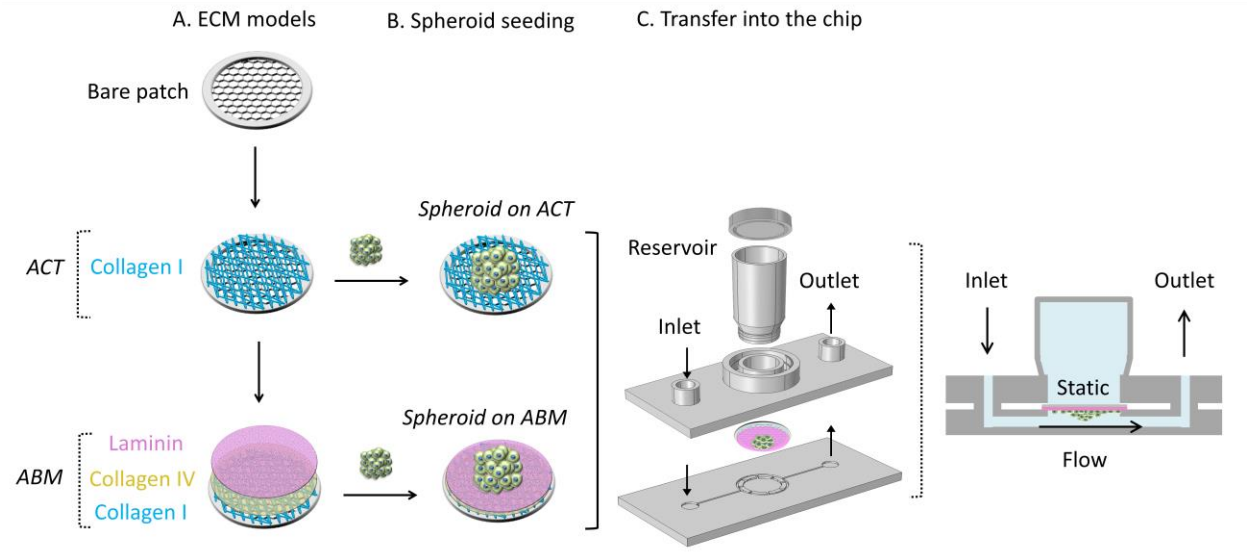

Figure 1. Scheme of the OC-chip. (A) ECM models: artificial connective tissues (ACT) and artificial basement membrane (ABM), (B) spheroids seeding, and (C) integration of the seeded ECM into the microfluidic chip.

2.3. Cell Culture

Human ovarian adenocarcinoma SKOV-3 cells (ATCC1, HTB77™) were purchased from ATCC (American Type Culture Collection, Manassas, VA). Cells were cultured in RPMI-1640 glutaMAX containing 0.07 % (v/v) sodium bicarbonate supplemented with 10% fetal bovine serum and 1% (v/v) penicillin streptomycin (all reagents were purchased from Thermo Fisher Scientific). Cells were cultured in T25 cell culture flasks in a humidified air atmosphere with 5% CO_2 at 37°C.

2.4. Spheroid growth

Ovarian tumor spheroid growth was performed with a high control over spheroid size, as recently described [20], and presented in detail in Supporting Information (Figure S2). Briefly, gelatin nanofibers were electrospun on caged-patch having a wall thickness of 200 µm. Then, agarose was coated on the gelatin fibers. After maintaining the spherical patch in the bottom of a 12-well plate using a PDMS ring, SKOV3 cells (4×10^5 cells/patch) were deposited on the caged-patch. After 3 days of culture, uniform spheroids were obtained with a diameter of *ca.* 200 µm. Ovarian tumor cells in spheroids were stained with epithelial (EpCAM and E-cadherin) and mesenchymal (Vimentin) markers (Figure S2).

2.5. Seeding ovarian tumor spheroids and integration in the microfluidic chip

Cell migration experiments were carried out on ACT and ABM and in static and flow conditions. First, all ECM models were sterilized by immersion in 70% ethanol for 5 min before washing in sterilized PBS 3 times for 5 min each time. The ACT/ABM supports were maintained at the bottom of the dish with a PDMS ring. Two to four SKOV3 tumor spheroids were selected using a micropipette and seeded one by one (Figure 1B). The tumor spheroids were incubated on the ECM models for 2 hours at 37°C and 5% CO_2. Similar experiments were also conducted with OVCAR-3 cells to study the impact of the ovarian cancer cell line (Figure S3-S4).

The seeded ECM was then transferred to a commercial microfluidic device (Mesobiotech, France) in an inverted configuration so that the spheroid was exposed to the flow (Figure 1C). The microfluidic device is composed of two plastic plates and a circular culture chamber (Ø 10 mm, h 1.5 mm) at the center of the chip (Figure 1C). The chip is closed with magnetic bounding and a mechanical clamper with four hand screws to prevent leakage for cell culture under flow for two days. The upper plate was designed to have two Luer connectors (one inlet and one outlet) and a central reservoir. The inlet channel is divided into six smaller channels to spill the flow into the central cavity while reducing the shear stress. The distribution of the shear rate (ν in s^{-1}) in the central cavity was simulated by computer fluid dynamics modeling for

two different flow rates and calculated to be $\nu \in (0.2\text{-}0.4\ s^{-1})$ at 20 $\mu L.min^{-1}$ and $\nu \in (1\text{-}2\ s^{-1})$ at 100 $\mu L.min^{-1}$ (see Supporting Information, Figure S5). Accordingly,

$$\tau = \nu \cdot \mu \qquad \text{(Eq.1)}$$

where τ is the shear stress and μ is the dynamic viscosity of the culture medium. Thus, $\tau \in (2.4\times10^{-3}\text{-}4.8\times10^{-3}\ dyn.cm^{-2})$ at 20 $\mu L.min^{-1}$ and $\tau \in (1.2\times10^{-2}\text{-}2.4\times10^{-2}\ dyn.cm^{-2})$ at 100 $\mu L.min^{-1}$, respectively, with a dynamic viscosity of 1.2×10^{-2} $dyn.s.cm^{-2}$. For the given channel with a section area in the central chamber of ~0.2×10 mm^2, a linear fluid velocity of ~0.2 and 0.8 $mm.s^{-1}$ can be obtained at a flow rate of 20 and 100 $\mu L.min^{-1}$ respectively, which also gives a shear rate in the order of the simulated values.

2.6. SEM imaging

For ECM characterization, samples were dried at 60°C overnight, then coated with gold for 60 s using an Emitech K675X Sputter Coater System with a sputtering current of 50 mA before imaging. Samples were fixed on conductive-tapes for imaging with a TM3030 Tabletop Microscope (Hitachi High-Technologies Corporation, Japan) working at an acceleration voltage of 15 kV.

2.7. Second harmonic generation / 2-photon excited fluorescence

We used a custom-built laser-scanning multiphoton microscope and recorded second harmonic generation (SHG) and 2-photon excited fluorescence (2PEF) images in parallel as previously described.[39] Excitation was provided by a femtosecond titanium–sapphire laser (Mai-Tai, Spectra-Physics) tuned to 860 nm, scanned in the XY directions using galvanometric mirrors and focused using a 25× with 1.05 NA objective lens (XLPLN25X-WMP2, Olympus), with a resolution of 0.35 µm (lateral) × 1.2 µm (axial) and a Z-step of 0.5 µm for the acquisition of Z-stack images. We used circular polarization to image all structures independently of their orientation in the image plane, using a 100 kHz acquisition rate, 420×420 nm^2 pixel size, and a typical power of 22 mW.

For the characterization of the basement membrane by 2PEF, ECM models were stained with Alexa Fluor 488®-conjugated collagen IV monoclonal antibody (eBioscience™, 53-9871-82) incubated overnight at

4°C or 2 h at room temperature at a concentration of 10 μg.mL^{-1}, together with laminin polyclonal primary antibody (Thermo Fisher Scientific, PA1-16730) for overnight at 4°C or 2 h at room temperature at a concentration of 1 μg.ml^{-1}, followed by 1 to 2 h incubation at room temperature with a goat–anti-rabbit-Alexa Fluor 610 secondary antibody at a dilution of 1/250.

2.8. Immunofluorescence and confocal image

After 2 days of culture, cells were fixed in 4% paraformaldehyde (PFA) in PBS for 10 minutes, and rinsed three times with PBS for 5 min each time. The cells were permeabilized with 0.5% Triton X-100 in PBS for 10 minutes, washed again 3 times in PBS, and saturated with PBS containing 3% BSA (with 0.1% Tween 20 and 0.1% sodium azide) for 30 min and washed again. Cells were then incubated overnight at 4°C with Alexa Fluor 543-conjugated vimentin antibody (ab202504, Abcam®) at a 1/1000 dilution and washed 3 times with PBS for 5 min each time to remove unbound vimentin conjugate. After washing, the actin cytoskeleton was stained with a 50 mg/mL Alexa Fluor 488 Phalloidin in PBS (containing 1% DMSO from the original stock solution, Abcam®) for 40 min at room temperature in a dark chamber. Cells were washed 3 times with PBS for 5 min each time to remove unbound phalloidin conjugate. Nuclear DNA was then stained with DAPI (4,6-diamidino-2-phenylindole dihydrochloride, Molecular Probe®) for 15 min at room temperature and washed again. For the 3D imaging of spheroids, cells were stained for nuclei with NucSpot® Live Cell Nuclear Stain. Immunofluorescent labeling was observed with a confocal microscope (LSM710, Zeiss) equipped with 405 (DAPI), 488 (phalloidin), and 543 (anti-vimentin antibody) nm lasers and with LSM ZEN 2009 software. We used 1 μm z-stack intervals and sequential scanning for each wavelength.

2.9. Image processing and statistical analysis

The migratory behavior (migrating distance, number of migrating cells, and core area) was analyzed using Image J [40]. The staining intensity of vimentin in the core and leading areas was analyzed using Image J by measuring the ratio of the integrated fluorescence intensity of a region of interest to the area of this region. More than 4000 cells were analyzed. Every group of experiments was run in triplicate and at least

9 tumor spheroids were statistically analyzed for each condition using the Two-Sample t-test. Finally, the morphology of cells and nuclei was analyzed by principal component analysis (PCA) using the CellTool software [41,42]. PCA allows the determination of the standard deviation (s.d.) that represents the square root of the total variance calculated from all the measured morphological features and hence quantifies the cellular heterogeneity.

3. Results

3.1. Impact of the ECM model on the migration of ovarian tumor spheroids

To construct the ovarian tumor-on-chip, porous supports with a diameter of 1.3 cm and a honeycomb micro-frame were fabricated that can be easily integrated into the circular chamber of our microfluidic device (Figure 1). The high porosity of the frame (400 µm-width honeycombs) ensures fluid exchanges and an important area of self-supporting tissue with limited mechanical contribution of the support (Figure 2). Two ECM models were selected to investigate the impact of key proteins in the OC environment (Figure 1A). The first one, referred to as artificial connective tissues (ACT) is made up of a fibrillar type I collagen network. This reproduces the late stage of OC, characterized by the loss of key proteins from the basement membrane. The second one is made up of a fibrillar network of type I collagen topped with type IV collagen and laminin to figure an artificial basement membrane (ABM). SEM imaging of the ACT shows the self-assembly of a dense layer of type I collagen fibers on the honeycomb microframe (Figure 2A1). For imaging the ECM in hydrated conditions, we used second harmonic generation (SHG), which is highly specific to the organization of collagen into densely packed triple helices. Figure 2A2 shows that the collagen I layer is homogeneous, with a thickness of a couple of microns. After adding successively type IV collagen and laminin, the layer thickness and aspect did not change under SEM (Figure 2B1). Combining SHG with 2-photon excited fluorescence (2PEF) allows us to specifically identify the presence of each protein: a top layer of laminin, with type IV collagen embedded within the ABM as observed on the different isolated channels (Figure S6). The stiffness of

ACT and ABM was measured by AFM nanoindentation, showing non-significant differences with mean values of 17 and 12 kPa for ACT and ABM respectively (Figure S7) [32].

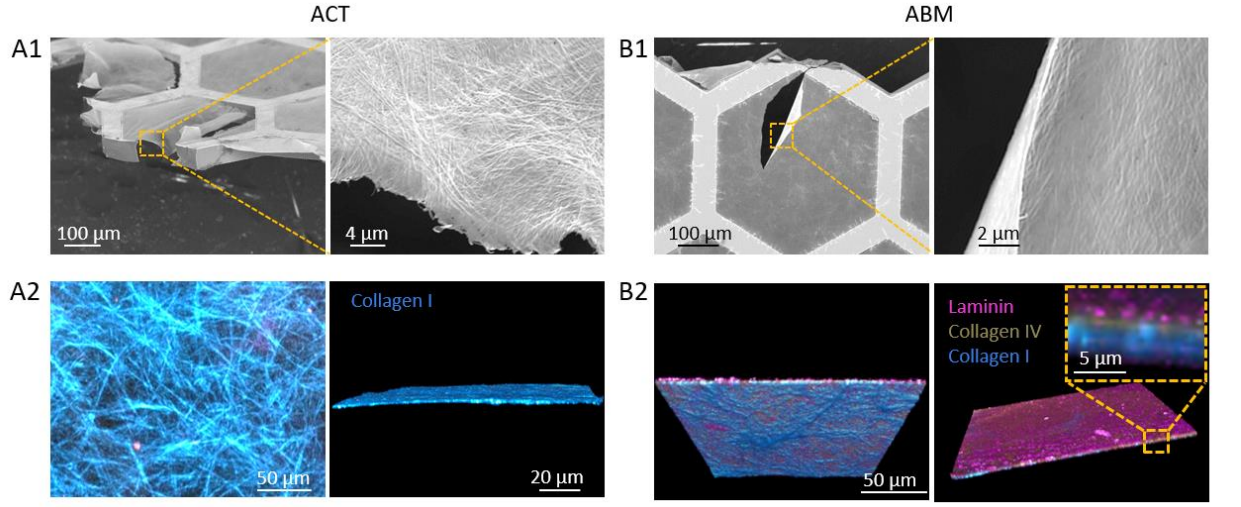

Figure 2. (A1, B1) SEM and (A2, B2) SHG/2-PEF images of (A) ACT and (B) ABM on honeycomb frame supports. Note that the image in B1 is a default that we attribute to the preparation of the sample for SEM, and that we have selected to better characterize the thickness of the sample.

Ovarian tumor spheroids (OTS) were grown on non-adherent supports until reaching a plain 3D structure with a uniform diameter of about 200 µm (Figure 3A and Figure S2) [20]. After three days, spheroids were taken out from the non-adherent support and seeded on ACT and ABM (Figure 3), and the impact of the ECM was evaluated in static conditions after immunofluorescence (IF) imaging. To quantify the migratory behavior, the mean migration distance, the number of migrating cells, and the core area were measured. We define the mean migration distance as the distance from the core to the front of the spheroid. Since the honeycomb frame has six-fold symmetry, we averaged the migration distance over 8 positions to account for the unsupported ECM and the frame (see yellow arrows in Figure 3A). The number of migrating cells was defined by the number of cells outside of the spheroid core, which could be automatically individualized for image analysis. On ACT models, the mean migration distance was found to be significantly higher than on ABM, and associated with a significantly lower number of migrating cells (Figure 3D,E). This signs for cells having higher motility and more individual migratory behavior on ACT compared to the collective migratory behavior on ABM in static conditions and shows that OC cells are strongly affected by the ECM. This is well-illustrated in Figure 3C-D, where a distinct

spheroid core with isolated surrounding cells can be observed on ACT contrary to the large growing core observed on ABM. Indeed, significantly smaller core areas of spheroids were measured on ACT compared to ABM (Figure 3G). Bright-field optical imaging can be found in Supporting Information to identify the evolution of the core from the onset of migration, just after spheroid seeding (Figure S8).

Zoom-in images in Figure 3 show the phenotypic variations of cells together with the variation of vimentin staining (in red). Vimentin is a cytoskeleton protein upregulated during cell transitioning events and commonly used as a mesenchymal marker [43-46]. E-cadherin and EpCAM were also systematically investigated as epithelial markers, staining cell-cell junctions (Figure S9). Typically, on both ECMs, cells in the core of spheroids were found to be round with a low expression of vimentin and become elongated from the core to the front of the spheroid, with increased expression of vimentin (Figure 3H). This expression pattern shows the prevalence of epithelial-type cells in the core of the OTS and evolving towards mesenchymal phenotypes at the migration front, which was enhanced for ABM compared to ACT (Figure 3H).

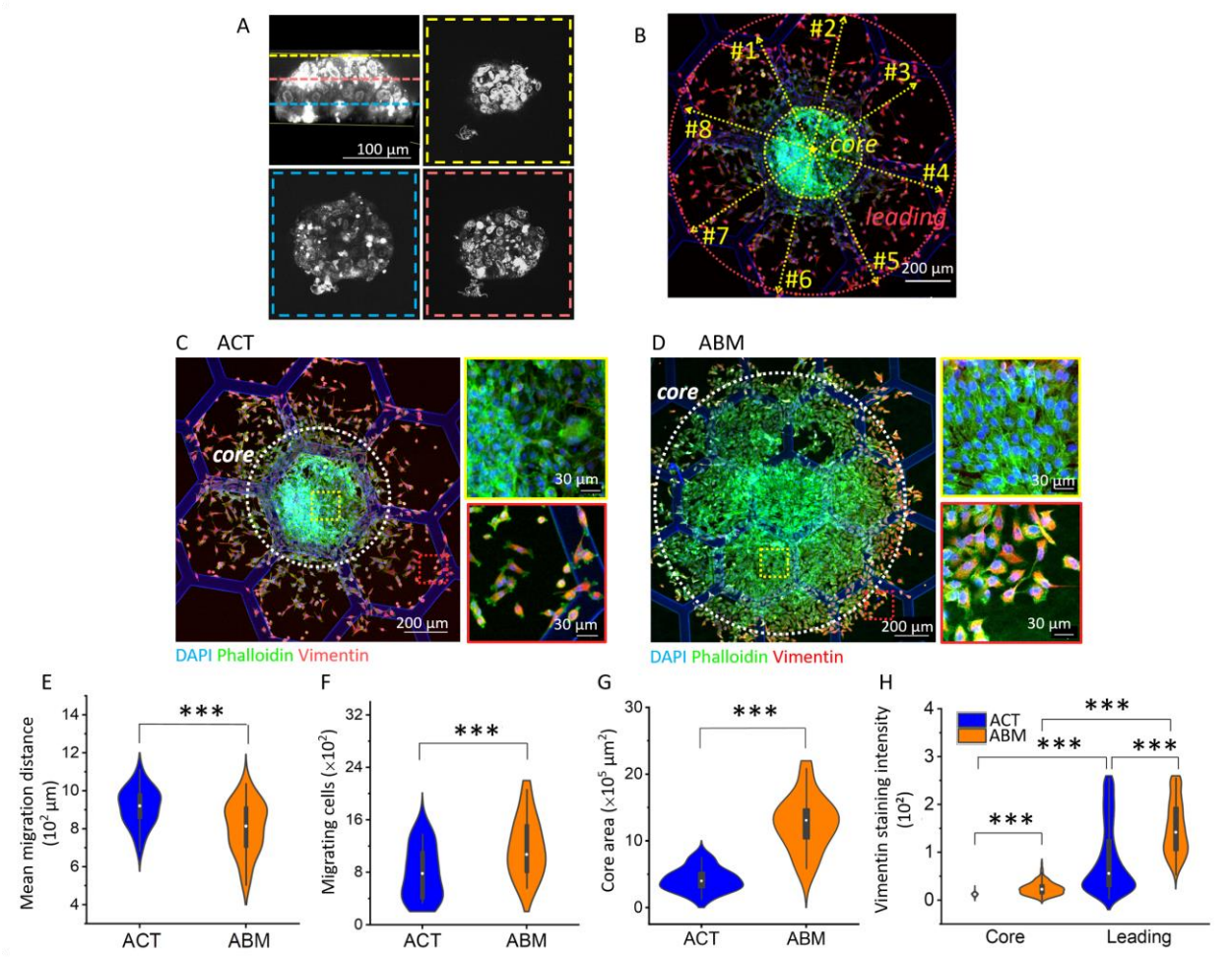

Figure 3. (A) 3D fluorescence imaging of spheroids before seeding on the ECM patch. Cells were stained for nuclei with NucSpot. (B) Schematic of the measurement of the mean migration distance, number of migrating cells, and core area. (C,D) IF imaging of SKOV-3 cells after 48 hours culture on ACT and ABM respectively. Cells were stained for vimentin (red), actin (green), and nuclei (DAPI, blue). (E-G) Plots of the mean migration distance, number of migrating cells, and core area on ACT and ABM models in static conditions. (H) Vimentin staining intensity as a function of cell positioning in the spheroid (***$p < 0.001$). Statistical analysis run over 9,441 cells on ACT and 12,929 cells on ABM.

We further analyzed the morphology of isolated cells (in the leading region) and their nuclei using principal component analysis (PCA) (Figure 4) [41,42]. PCA provides information about the number of geometrical descriptors -*shape modes*- that account for the morphological heterogeneity of a population of cells/nuclei. In addition, for each descriptor, it gives the distribution of values associated with standard deviations. In the analysis, we only accept components that account for more than 5% of variability. Cell morphology, based on the staining of the actin cytoskeleton, reveals two shape modes on ACT and ABM (Figure 4A). The most important geometrical descriptor for both cell populations is the elongation of cell

shape, being more elongated for cells on ACT than on ABM, and with larger size. Nuclei were also found to be more elongated on ACT than on ABM in static conditions, with smaller sizes (Figure 4B).

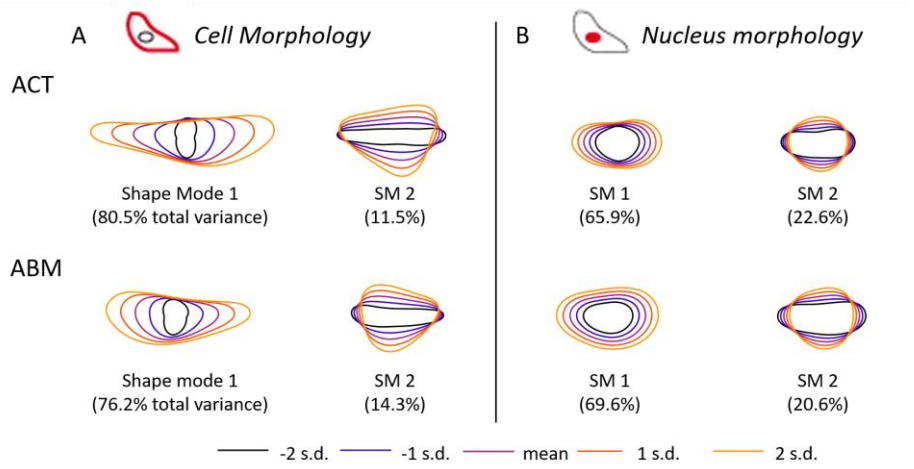

Figure 4. PCA of nucleus and cell morphology 48h after seeding on the different ECMs in static conditions: (A) morphological variance of cell morphology based on phalloidin staining of the actin cytoskeleton and (B) morphological variance of nucleus morphology based on DAPI staining. The color code is common to all plots. s.d. is for standard deviation, as determined by PCA for the quantification of the variance in the measured morphological features. Morphological analysis was run over 1,358 cytoskeletons (actin) and 1,120 nuclei on ACT and over 1,261 cytoskeletons (actin) and 2,567 nuclei on ABM.

3.2. Effect of fluid shear stress on ovarian tumor cells cultured on ACT

After the identification of ECM impact on SKOV-3 spheroid behavior, we added up a flow to make cells experience the fluid shear stress of the peritoneal cavity. Compared to the conventional approach relying on cell culture with an already integrated membrane, we use a “seeding first and insert after” approach, where the culture support engineered with the ECM and seeded with OTS is inserted in the central chamber of the chip (Figure 1). This also allows easy removal of the culture support for downstream IF observations. Two perfusion speeds were selected to match the physiological shear stress measured in dyn/cm² for biological applications which depend on cavity and vessel types, being less than a $dyn.cm^{-2}$ in the peritoneal cavity. Perfusion speeds of 20 and 100 $\mu L.min^{-1}$ were calculated to give shear stress values in the range of 10^{-3} and 10^{-2} $dyn.cm^{-2}$ respectively, which correspond to values of shear on cells of about 0.2 and 0.8 $mm.s^{-1}$. Preliminary experiments were implemented to confirm that under these shear rates, no significant impact on the structure and composition of the ECM models could be observed (Figure S10).

In both conditions, the individual migration mode observed under static conditions was confirmed. Spheroids show a small and dense core with isolated cells migrating towards the front (Figure 5A,B). The mean migration distance and number of migrating cells were found to decrease with increasing shear stress, together with a smaller area of the spheroid core (Figure 5C-E). Regarding the intensity of vimentin staining, an important increase was again observed from the spheroid cores to the front, whatever the shear stress (Figure 5F). This signs for the acquisition of mesenchymal markers in the course of migration. No increase in vimentin staining could be measured in the core upon increasing the shear stress. However, the intensity of vimentin staining in the leading area of the spheroid was found to be significantly enhanced upon increasing the shear stress (Figure 5F). The impact of shear stress on individual migration mode on ACT was found to increase with increasing shear stress. In particular, we observe an important shrinking of the core, together with an important increase in vimentin expression for the leader cells out of the core area. This signs for more aggressive cells with higher motility in the presence of higher shear stress.

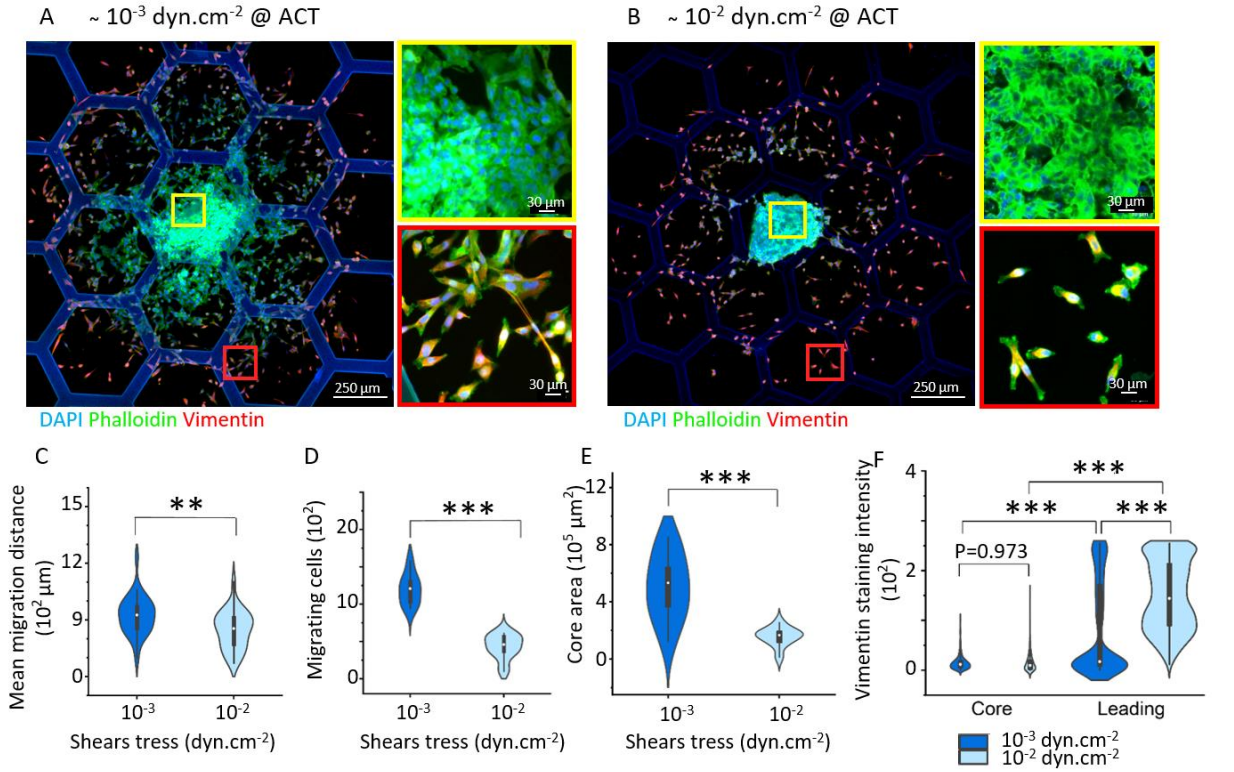

Figure 5. Effects of flow shear stress on the migration of SKOV-3 cells on ACT. (A, B) IF imaging of SKOV-3 cells after 48 hours culture on ACT. Cells were stained for vimentin (red), actin (green), and nuclei (DAPI, blue). (C-E) Plots of the mean migration distance, number of migrating cells, and core area on ACT as a function of shear stress. (F) Vimentin staining intensity as a function of cell positioning in the spheroid and shear stress (**p <0.01; ***p < 0.001). Statistical analysis run over 9,610 cells at 10^{-3} dyn.cm^{-2}, and 5,932 cells at 10^{-2} dyn.cm^{-2}.

The quantification of morphological descriptors was performed on isolated cells. PCA revealed that both cells and nuclei decrease in size while being more elongated when increasing the shear stress from 10^{-3} to 10^{-2} dyn.cm^{-2} (Figure 6).

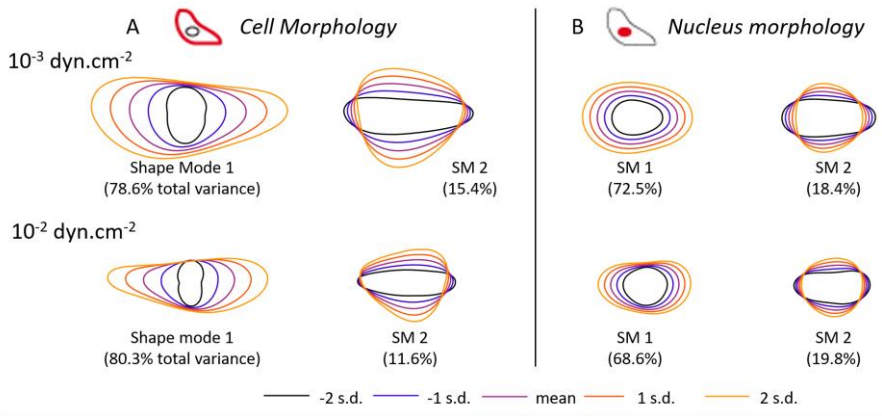

Figure 6. PCA of nucleus and cell morphology 48h after seeding on ACT as a function of flow shear stress: (A) morphological variance of cell morphology based on phalloidin staining of the actin cytoskeleton and (B) morphological variance of nucleus morphology based on DAPI staining. The color code is common to all plots. s.d. is for standard deviation, as determined by PCA for the quantification of the variance in the measured morphological features. Morphological analysis was run over 1,358 cytoskeletons (actin) and 1,631 nuclei at 10^{-3} dyn.cm^{-2} and over 1,351 cytoskeletons (actin) and 878 nuclei at 10^{-2} dyn.cm^{-2}.

3.3. Effect of fluid shear stress on ovarian tumor cells cultured on ABM

SKOV-3 spheroids were finally seeded on ABM and cultured under flow at 10^{-3} to 10^{-2} dyn.cm^{-2} for two days. The collective migration observed under static conditions was confirmed under flow, with large spheroids surrounded by a few isolated cells (Figure 7A,B). While the mean migration distance was found to slightly increase with the shear stress, the number of migrating cells and core area were not significantly affected indicating a limited impact of the shear stress on the migration behavior of OC cells cultured on ABM (Figure 7C-E). The staining intensity of vimentin was found to again increase from the core to the leading area of the spheroid but with a rather limited increase in the leading region with the shear stress compared to the increase observed on the ACT scaffold (Figure 7F).

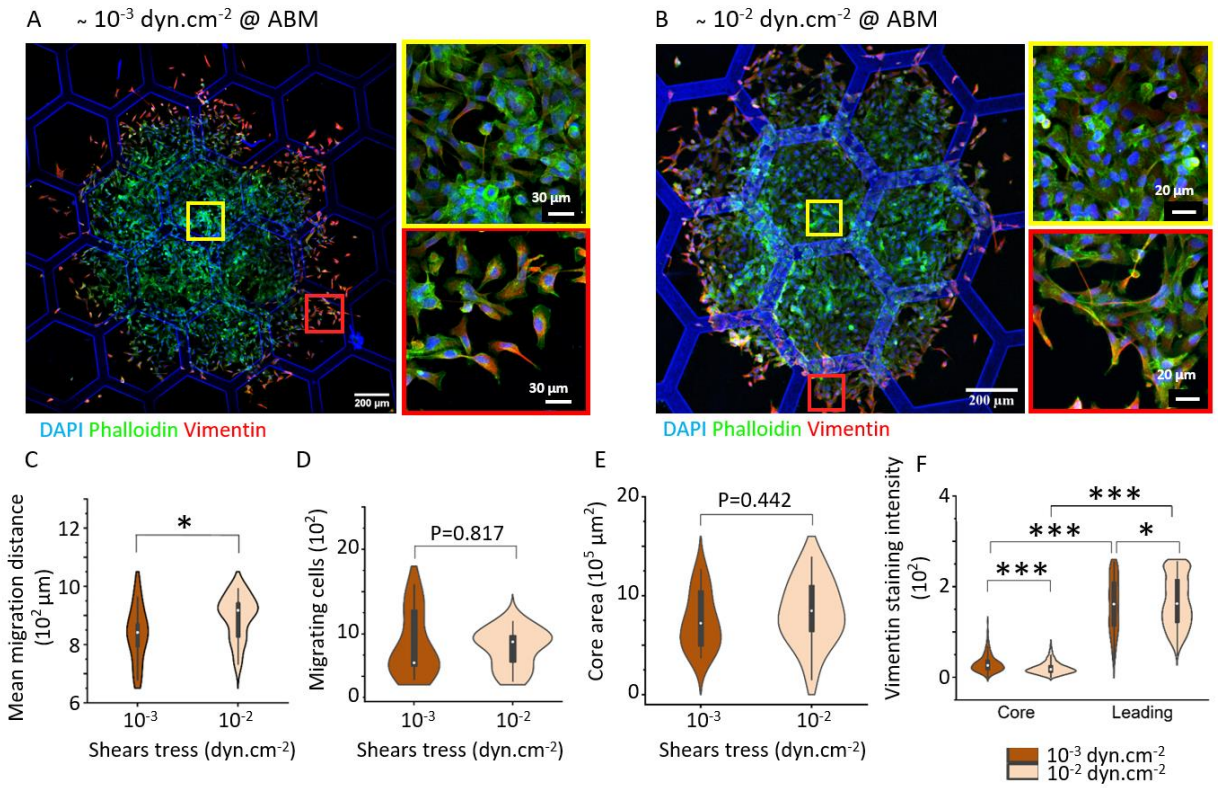

Figure 7. Effects of flow shear stress on the migration of SKOV-3 cells on ABM. (A,B) IF imaging of SKOV-3 cells after 48 hours culture on ABM. Cells were stained for vimentin (red), actin (green), and nuclei (DAPI, blue). (C,E) Plots of the mean migration distance, number of migrating cells, and core area on ABM as a function of shear stress. (F) Vimentin staining intensity as a function of cell positioning in the spheroid and shear stress (*p <0.05; ***p < 0.001). Statistical analysis run over 9,466 cells at 10^{-3} dyn.cm^{-2}, and 14,178 cells at 10^{-2} dyn.cm^{-2}.

Finally, the morphological variations of cells and nuclei upon increasing shear stress were quantified by PCA analysis. Upon increasing the shear rate from 10^{-3} to 10^{-2} dyn.cm^{-2}, cells were found to become rounder with smaller nuclei.

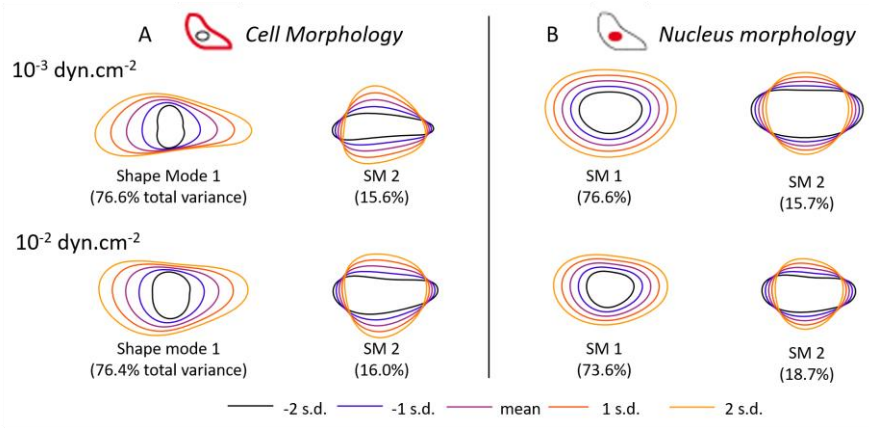

Figure 8. PCA of nucleus and cell morphology 48h after seeding on ABM as a function of flow shear stress: (A) morphological variance of cell morphology based on phalloidin staining of the actin cytoskeleton and (B) morphological variance of nucleus morphology based on DAPI staining. The color code is common to all plots. s.d. is for standard deviation, as determined by PCA for the quantification of the variance in the measured morphological features. Morphological analysis was run over 1,887 cytoskeletons (actin) and 1,941 nuclei at 10^{-3} dyn.cm^{-2} and over 2,830 cytoskeletons (actin) and 3,068 nuclei at 10^{-2} dyn.cm^{-2}.

3.4. Effect of fluid shear stress on the directionality of migration

The effect of the direction of the fluid shear stress imposed in the chip has been evaluated using Fidji. The angle of the main axis of migrating cells, *i.e.* in their largest dimension, to a defined angle of the chip was extracted and the Kernel distribution plotted (Figure 9, angle scaling from 0 to 180°). The angle is irrespective of the flow shear stress because the patch was taken out of the chip for imaging and this approach should be refined in future works. For one spheroid in a given condition, an average angle of 0° describes an isotropic migration, *i.e.* with no preferred cell orientation. Let's first take a look at the angle distribution of cells seeded on ACT with increasing shear stress, from static to 10^{-2} dyn.cm^{-2}, with a focus on the variation of cellular angle distribution from one spheroid to another in the same condition (Figure 9A1-3). In the absence of flow, the angle distribution is centered around 0° with limited variation from one spheroid to another (Figure 9A1). At shear stress in the 10^{-3} dyn.cm^{-2} range, a similar behavior is observed, with angle dispersion centered around 0° (Figure 9A2). A distinct behavior is observed upon increasing shear stress up to 10^{-2} dyn.cm^{-2}: a slight shift above 0° is observed with reproducible behavior from one spheroid to another one (with p-value > 0.95, Figure 9A3). This is attributed to the induction of directionality of cell migration on ACT upon increasing the flow-shear stress in the 10^{-2} dyn.cm^{-2} range. A distinct behavior is observed for cells seeded on ABM. The angular distribution is centered around 0° in static conditions as well as with increasing shear stress. This signs for an isotropic orientation of cells (Figure 9B1-3).

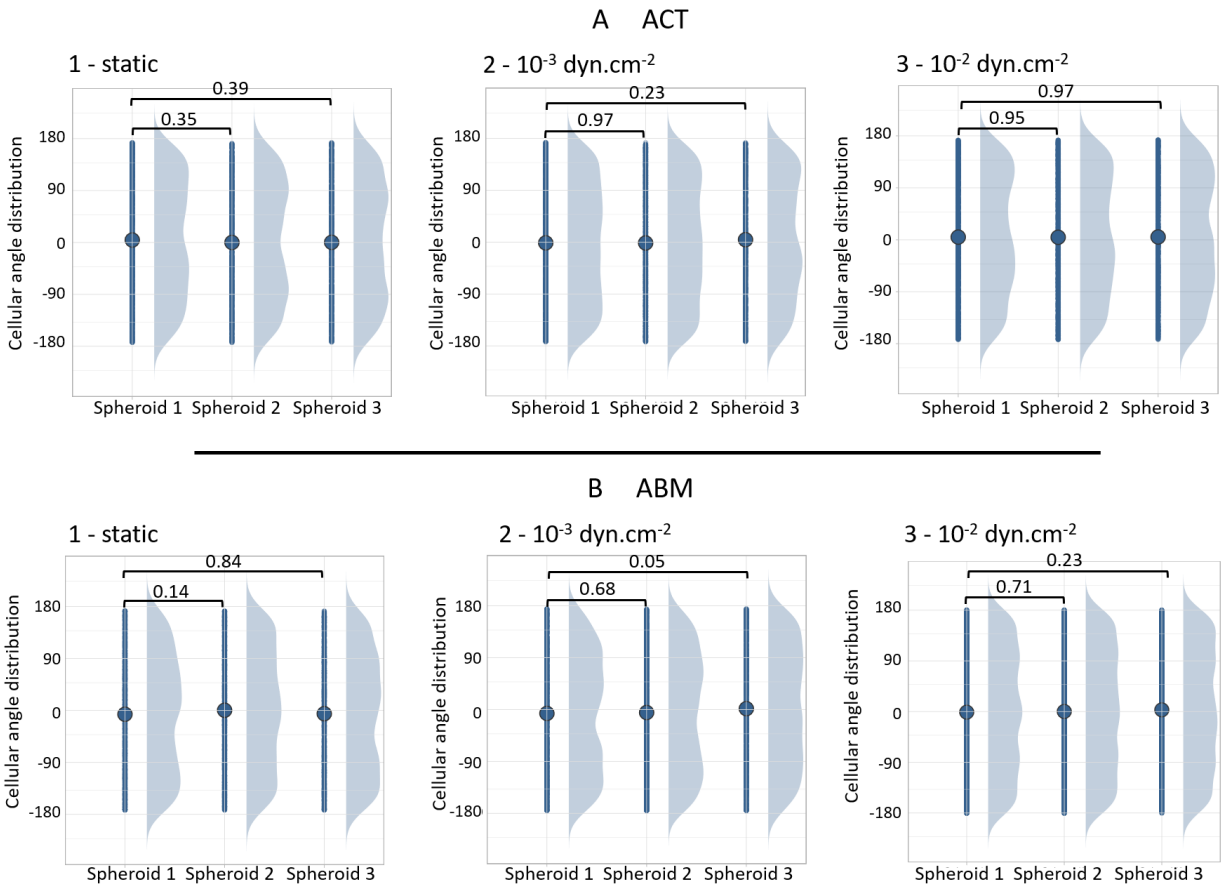

Figure 9. Kernel density estimation of the orientation of cells for three spheroids per condition as a function of shear stress: (A) ACT and (B) ABM (1) in the absence of shear stress - static conditions -, in the range of (2) 10^{-3} dyn.cm^{-2}, and (3) 10^{-2} dyn.cm^{-2}. On ACT, the angular distribution analysis was run over 1,384 cells in static condition (542, 435, and 407 cells per spheroid); 1,575 cells (585, 586, 404 cells per spheroid) at 10^{-3} dyn.cm^{-2} and 1,367 cells (516, 426, 425 cells per spheroid) 10^{-2} dyn.cm^{-2}. On ABM, the analysis was run over 1,338 cells in static condition (480, 410, and 448 cells per spheroid); 1,950 cells (634, 809, 507 cells per spheroid) at 10^{-3} dyn.cm^{-2} and 2,979 cells (950, 1094, 935 cells per spheroid) 10^{-2} dyn.cm^{-2}. Angles have been extracted using Fidji software.

4. Discussion

Migratory behavior. Invasive tissue migration, *via* metastasis, is a mortality factor in cancer. After seeding on ECM models, ovarian tumor spheroids migrated from the center of the spheroid. The migratory behavior was evaluated by measuring the distance of migration and the number of individual migrating cells out of the core of the spheroid and the core area. All of these descriptors were found to be strongly affected by the composition of the ECM model made up of collagen 1-based connective tissues (ACT) topped or not with a basement membrane from type IV and laminin (ABM). Because these two

proteins are degraded in the course of ovarian cancer, these two ECMs reproduce the late and early stages of ovarian cancer progression respectively. An individual migration mode, characterized by a small area of the spheroid core and numerous individual migrating cells was observed on ACT, while a more collective behavior was observed for an early migration stage, on the ABM (Figure 10A). In this case, large spheroid cores with a limited number of individual cells were observed. This highlights the importance of considering the nature of ECM to elaborate models. Increased migration is often associated with an increase in stiffness in collagen or collagen-Matrigel mixture [30,31,47]. In our work, the stiffness of ACT and ABM, as measured by AFM nanoindentation, showed non-significant differences with mean values of 17 and 12 kPa for ACT and ABM respectively (Figure S7) [32]. The difference in migratory behavior is rather attributed here to the cell-ECM interactions in the presence of type IV collagen and laminin in the ABM model and the ability of this high-density coating of retaining factors from the culture medium as previously observed with Matrigel [30,31].

Interestingly, this strong difference in migration behavior depending on the ECM model was preserved under flow conditions. Individual migration with a decreasing area of spheroid core was observed on ACT with an increasing flow rate, while a large core characteristic of a more collective migration mode was observed whatever the shear stress. This is consistent with the activation of integrins and focal adhesions in mechanotransduction pathways governing cell migration under flow shear stress [48]. This should account for the dominance of adhesion in regulating cell migration in the course of ECM remodeling during cancer progression, beyond its stiffening, with the loss of the basement membrane [49].

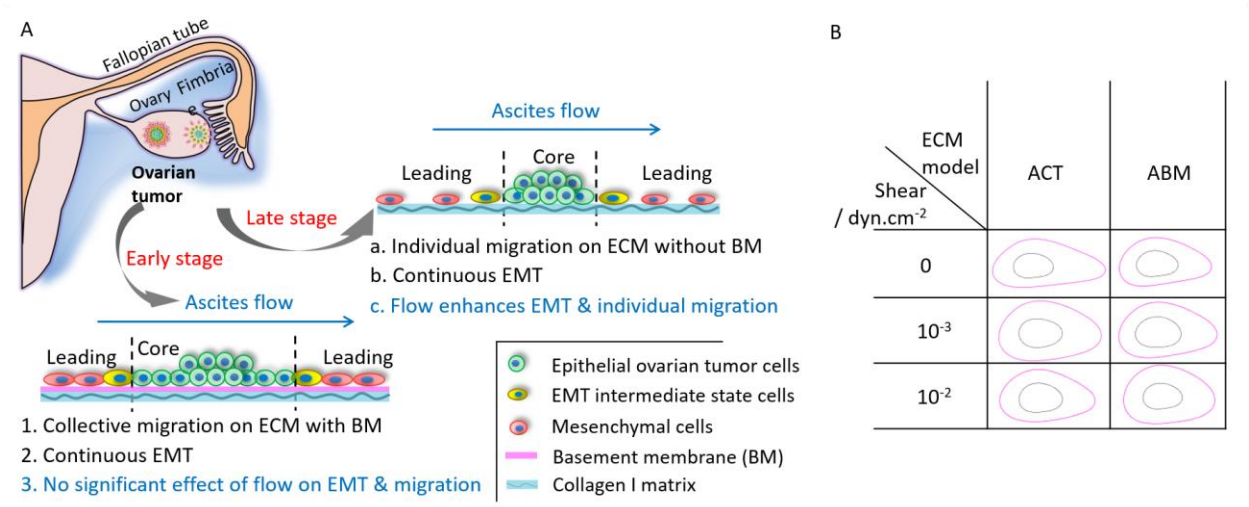

Figure 10. (A) Scheme of the effect of ECM remodeling and flow shear stress on the EMT and metastasis of OC cells. (B) Scheme of nucleus and cell morphology evolution of SKOV-3 cells on ACT and ABM in different shear stress conditions.

Cytoskeleton reorganization and morphology. The intensity of vimentin staining was found to increase from the core to the leading area in all conditions, whatever the ECM model and shear stress applied. This illustrates the reorganization of the cytoskeleton of epithelial-type cells in the core of the spheroid transitioning towards mesenchymal-type cells with enhanced migratory properties. Interestingly, flow shear stress enhances vimentin staining in SKOV-3 cells seeded on ACT, while a limited effect could be measured on ABM. In terms of morphology, a high dependency on ECM was observed in static conditions, with cells being larger and more elongated on ACT than on ABM. Under flow, variations in cell morphologies were found to be lowered, and cells became smaller and rounder on both ECMs compared to the static conditions (Figure 9B). It is worth mentioning that from 10^{-3} to 10^{-2} dyn.cm^{-2}, ACT cells preserve an elongated shape.

Overall, the ECM plays a crucial role in determining whether ovarian cancer cells migrate individually or collectively. The addition of fluid-induced shear stress confirmed the migration pattern observed under static conditions. This highlights the central role of the ECM in the presence of physiological shear force. Interestingly, the flow had a different impact on cell migration depending on the nature of the ECM. On ACT, shear stress enhanced individual migration, with a decrease in the spheroid core area and an increase in the intensity of vimentin staining. This is attributed to the individual state of the cells, which

are exposed to shear over their entire surface, and are all affected in the same way. In contrast, a limited impact of shear stress was observed on the collective migration mode observed on ABM. This is explained by the self-protective features of collective assemblies, where the cells in the spheroid core are protected by surrounding cells, which are themselves less exposed to shear due to enhanced cell-cell interactions.

The ability of our models not only to discriminate between ECM and flow shear stress, but also to investigate both factors synergistically is an important asset as flow shear stress has been studied with little attention to ECM evolution. Indeed, ECM and flow have rarely been combined in the literature to study the impact of ECM properties on cells in integrated systems, despite the importance of work on the impact of ECM on the behavior of (cancer) cells in static contexts. This is a crucial step towards the improvement of *in vitro* models of biological relevance, given the importance of the ECM in cell behavior. This has been made possible here by the ability to adjust the properties of the ECM upstream of the chip, using the "seeding first and insert after" approach, where the ECM is prepared before being integrated into the chip. Importantly, this implies that there are no constraints in terms of process or matrix composition. While physiological 3D models of connective tissues [48,50], including those using Matrigel [31], have been combined with flow shear stress, the use of a controlled number, concentration and organization of several ECM components (type I and type IV collagen, laminin) considerably refines the model, particularly for studying cancer at different stages. In the specific case of ovarian cancer, previous studies have shown the impact and degradation of laminin and type IV collagen as an important marker of cancer progression, but to our knowledge, no *in vitro* model has been constructed from these *ex vivo* tissue analyses to reproduce this particular context. Finally, it is important to mention here the fact that we can reach the physiological mechanical properties of healthy and cancer tissues in our setup, thanks to the use of a porous honeycomb structure, which provides a large surface area of self-supporting tissue. This is necessary to study the impact of ECM properties on cells. This makes it possible to get rid of the mechanical properties of the support, which are known to impact cell behavior, but which is rarely achieved in literature. In addition to these materials considerations, the addition of flow is of utmost

importance and a key parameter to hold when designing relevant therapeutic models, given the reported impact of flow in therapeutic resistance in ovarian cancer [51].

5. Conclusion

We have built an easy-to-handle ovarian tumor-on-chip to reproduce the ECM environment and ascitic flow conditions during ovarian cancer. This device highlights the importance of key basement membrane proteins, type IV collagen, and laminin, in the migratory behavior of cells. Indeed, ECM was found to prevail over shear stress in the physiological range of the peritoneal cavity in determining the individual or collective migratory behavior of ovarian cancer cells. Collective migration was observed on early-stage ECM, while a more individual migration was observed at a later stage correlating with BM degradation. Furthermore, the application of shear stress did not have the same impact on migration depending on the ECM, with aggressive individual migration being enhanced by shear, while a limited impact was observed on more collective migrations. This work highlights the need to take ECM and its synergy with flow shear stress into account when studying cell migration, and even more so when developing tumor microenvironments-on-chip. The use of multiple ECM components has rarely been considered so far and will be of paramount importance in the study of cancer stage progression for academic research and therapeutic developments.

Credit author statement

Declaration of competing interest

Acknowledgments

We thank the China Scholarship Council for the PhD grant of Changchong Chen; Rachele Allena and Nicolas Ruyssen for their help with shear stress simulations; Christophe Hélary and Gervaise Mosser for their help in the extraction and purification of type I collagen, and Clothilde Raoux for her constant support with SHG/2PEF experiments, and Tristan Piolot for AFM nanoindentation experiments. This project has received financial support from the CNRS through the MITI interdisciplinary programs. Multiphoton imaging at LOB was partly supported by the Agence Nationale de la Recherche (contracts ANR-11-EQPX-0029 Morphoscope2 and ANR-10-INBS-04FBI). This work benefited from the technical

contribution of the Institut Pierre-Gilles de Gennes joint service unit CNRS UAR 3750. The authors would like to thank the engineers of this unit for their advice during the development of the experiments: Bertrand Cinquin, Nhung Dinh, Audric Jan, Kévin Phan. We thank members of the MEC-uP Team for helpful discussions and comments. This work was funded by ANR JCJC Modulo-EMT ANR-21-CE19-0006 and is a part of Alphonse Boché doctoral work.

References

[1] PDQ Adult Treatment Editorial Board. Ovarian Epithelial, Fallopian Tube, and Primary Peritoneal Cancer Treatment (PDQ®): Health Professional Version. 2023 Mar 14. In: PDQ Cancer Information Summaries [Internet]. Bethesda (MD): National Cancer Institute (US); 2002-. Available from: https://www.ncbi.nlm.nih.gov/books/NBK66007/

[2] E. Lengyel, Ovarian cancer development and metastasis, Am. J. Pathol. 177 (2010) 1053-1064.

[3] C. Novak, E. Horst, G. Mehta, Review: Mechanotransduction in ovarian cancer: Shearing into the unknown, APL Bioeng. 2 (2018) 031701.

[4] R. Kalluri, R.A. Weinberg, The basics of epithelial-mesenchymal transition, J. Clin. Invest. 119 (2009) 1420-1429.

[5] M.A. Huber, N. Kraut, H. Beug, Molecular requirements for epithelial-mesenchymal transition during tumor progression. Curr. Opin. Cell Biol. 17 (2006) 548-558

[6] I.H. Roland, W.-L. Yang, D.-H. Yang, M.B. Daly, R.F. Ozols, T.C. Hamilton, H.T. Lynch, A.K. Godwin, X.-X. Xu, Loss of surface and cyst epithelial basement membranes and preneoplastic morphologic changes in prophylactic oophorectomies, Cancer 98 (2003) 2607-2623.

[7] O. Nadiarnykh, R.B. LaComb, M.A. Brewer, P.J. Campagnola, Alterations of the extracellular matrix in ovarian cancer studied by Second Harmonic Generation imaging microscopy, BMC Cancer 10 (2010) 94.

[8] N.D. Kirkpatrick, M.A. Brewer, U. Utzinger, Endogenous optical biomarkers of ovarian cancer evaluated with multiphoton microscopy, Cancer Epidemiol Biomarkers Prev. 16 (2007) 2048-2057.

[9] K. Song, Z. Wang, R. Liu, G. Chen, L. Liu, Microfabrication-Based Three-Dimensional (3-D) Extracellular Matrix Microenvironments for Cancer and Other Diseases, Int. J. Mol. Sci. 19 (2018) 935.

[10] L. Carduner, C.R. Picot, J. Leroy-Dudal, L. Blay, S. Kellouche, F. Carreiras, Cell cycle arrest or survival signaling through αv integrins, activation of PKC and ERK1/2 lead to anoikis resistance of ovarian cancer spheroids, Exp. Cell Res. 320 (2014) 329-342.

[11] S. Raghavan, P. Mehta, M.R. Ward, M.E. Bregenzer, E.M.A. Fleck, L. Tan, K. McLean, R.J. Buckanovich, G. Mehta, Personalized Medicine-Based Approach to Model Patterns of Chemoresistance and Tumor Recurrence Using Ovarian Cancer Stem Cell Spheroids, Clin. Cancer Res. 23 (2017) 6934-6945.

[12] N. Casagrande, C. Borghese, F. Agostini, C. Durante, M. Mazzucato, A. Colombatti, D. Aldinucci, In Ovarian Cancer Multicellular Spheroids, Platelet Releasate Promotes Growth, Expansion of ALDH+ and CD133+ Cancer Stem Cells, and Protection against the Cytotoxic Effects of Cisplatin, Carboplatin and Paclitaxel, Int. J. Mol. Sci. 22 (2021) 3019.

[13] L.B. Weiswald, D. Bellet, V. Dangles-Marie, Spherical Cancer Models in Tumor Biology, Spherical cancer models in tumor biology, Neoplasia 17 (2015) 1-15.

[14] C. Kim, K.S. Lee, J.H. Bang, Y.E. Kim, M.C. Kim, K.W. Oh, S.H. Lee, J.Y. Kang, 3-Dimensional Cell Culture for on-Chip Differentiation of Stem Cells in Embryoid Body, Lab Chip 11 (2011) 874-882.

[15] C. Kim, J.H. Bang, Y.E. Kim, S.H. Lee, J.Y. Kang, On-Chip Anticancer Drug Test of Regular Tumor Spheroids Formed in Microwells by a Distributive Microchannel Network, Lab Chip 12 (2012) 4135-4142.

[16] Y.C. Chen, X. Lou, Z. Zhang, P. Ingram, E. Yoon, E. High-Throughput Cancer Cell Sphere Formation for Characterizing the Efficacy of Photo Dynamic Therapy in 3D Cell Cultures, Sci. Rep. 5 (2015) 12175.

[17] N. Dadgar, A.M. Gonzalez-Suarez, P. Fattahi, X. Hou, J.S. Weroha, A. Gaspar-Maia, G. Stybayeva, A. Revzin, A Microfluidic Platform for Cultivating Ovarian Cancer Spheroids and Testing Their Responses to Chemotherapies, Microsyst. Nanoeng. 6 (2020) 93.

[18] R. Foty, A Simple Hanging Drop Cell Culture Protocol for Generation of 3D Spheroids, J. Vis. Exp. 51 (2011) e2720.

[19] T. Das, L. Meunier, L. Barbe, D. Provencher, O. Guenat, T. Gervais, A.M. Mes-Masson, Empirical Chemosensitivity Testing in a Spheroid Model of Ovarian Cancer Using a Microfluidics-Based Multiplex Platform, Biomicrofluidics 7 (2013) 011805.
[20] C. Chen, Y. He, E. Lopez, F. Carreiras, A. Yamada, M.-C. Schanne-Klein, A. Lambert, Y. Chen, C. Aimé, High-throughput tuning of ovarian cancer spheroids for on-chip invasion assays, Micro and Nano Engineering 15 (2022) 100138.
[21] S.S. Li, C.K.M. Ip, M.Y.H. Tang, S.K.H. Sy, S. Yung, T.M. Chan, M. Yang, H.C. Shum, A.S.T. Wong, Modeling Ovarian Cancer Multicellular Spheroid Behavior in a Dynamic 3D Peritoneal Microdevice, J. Vis. Exp. 120 (2017) 55337.
[22] I. Rizvi, U.A. Gurkan, S. Tasoglu, N. Alagic, J.P. Celli, L.B. Mensah, Z. Mai, U. Demirci, T. Hasan, Flow Induces Epithelial-Mesenchymal Transition, Cellular Heterogeneity and Biomarker Modulation in 3D Ovarian Cancer Nodules, Proc. Natl. Acad. Sci. U S A 110 (2013) E1974-83.
[23] A.R. Hyler, N.C. Baudoin, M.S. Brown, M.A. Stremler, D. Cimini, R.V. Davalos, E.M. Schmelz, Fluid Shear Stress Impacts Ovarian Cancer Cell Viability, Subcellular Organization, and Promotes Genomic Instability. PLoS One 13 (2018) 1-21.
[24] L. Avraham-Chakim, D. Elad, U. Zaretsky, Y. Kloog, A. Jaffa, D. Grisaru, Fluid-Flow Induced Wall Shear Stress and Epithelial Ovarian Cancer Peritoneal Spreading, PLoS One 8 (2013) e60965.
[25] C.K.M. Ip, S.S. Li, M.Y.H. Tang, S.K.H. Sy, Y. Ren, H.C. Shum, A.S.T. Wong, Stemness and Chemoresistance in Epithelial Ovarian Carcinoma Cells under Shear Stress, Sci. Rep. 6 (2016) 26788.
[26] A.A. Hassan, M. Artemenko, M.K. Tang, Z. Shi, L.-Y. Chen, H.-C. Lai, Z. Yang, H.-C. Shum, A.S.T. Wong, Ascitic Fluid Shear Stress in Concert with Hepatocyte Growth Factor Drive Stemness and Chemoresistance of Ovarian Cancer Cells via the C-Met-PI3K/Akt-MiR-199a-3p Signaling Pathway, Cell Death Dis. 13 (2022) 537.
[27] B. Saha, T. Mathur, K.F. Handley, W. Hu, V. Afshar-Kharghan, A.K. Sood, A. Jain, OvCa-Chip microsystem recreates vascular endothelium-mediated platelet extravasation in ovarian cancer, Blood Adv. 4 (2020) 3329-3342.
[28] B. Saha, T. Mathur, J.J. Tronolone, M. Chokshi, G.K. Lokhande, A. Selahi, A.K. Gaharwar, V. Afshar-Kharghan, A.K. Sood, G. Bao, A. Jain, Human tumor microenvironment chip evaluates the consequences of platelet extravasation and combinatorial antitumor-antiplatelet therapy in ovarian cancer, Sci. Adv. 7 (2021) eabg5283.
[29] L.I. Ibrahim, C. Hajal, G.S. Offeddu, M.R. Gillrie, R.D. Kamm, Omentum-on-a-chip: A multicellular, vascularized microfluidic model of the human peritoneum for the study of ovarian cancer metastases, Biomaterials, 288 (2022) 121728.
[30] M. Anguiano, X. Morales, C. Castilla, A. Rodríguez Pena, C. Ederra, M. Martínez, M. Ariz, M. Esparza, H. Amaveda, M. Mora, N. Movilla, J.M. García Aznar, I. Cortés-Domínguez, C. Ortiz-de-Solorzano, The use of mixed collagen-Matrigel matrices of increasing complexity recapitulates the biphasic role of cell adhesion in cancer cell migration: ECM sensing, remodeling and forces at the leading edge of cancer invasion, PLoS ONE, 15 (2020) e0220019.
[31] M. Anguiano, C. Castilla, M. Maška, C. Ederra, R. Peláez, X. Morales, G. Muñoz-Arrieta, M. Mujika, M. Kozubek, A. Muñoz-Barrutia, A. Rouzaut, S. Arana, J.M. Garcia-Aznar, C. Ortiz-de-Solorzano, Characterization of three-dimensional cancer cell migration in mixed collagen-Matrigel scaffolds using microfluidics and image analysis, PLoS ONE, 12 (2017) e0171417.
[32] C. Chen, Z. Ibrahim, M.F. Marchand, T. Piolot, S. Kamboj, F. Carreiras, A. Yamada, M.-C. Schanne-Klein, Y. Chen, A. Lambert, C. Aimé, 3D collagen topology shapes cell morphology, beyond stiffness, ACS Biomater Sci Eng. 8 (2022) 5284-5294.
[33] L. Liu, K.-I. Kamei, M. Yoshioka, M. Nakajima, J. Li, N. Fujimoto, S. Terada, Y. Tokunaga, Y. Koyama, H. Sato, K. Hasegawa, N. Nakatsuji, Y. Chen, Nano-on-micro fibrous extracellular matrices for scalable expansion of human ES/iPS cells, Biomaterials, 124 (2017) 47-54.
[34] Y. Tang, L. Liu, J. Li, L. Yu, F.P.U. Severino, L. Wang, J. Shi, X. Tu, V. Torre, Y. Chen, Effective motor neuron differentiation of hiPSCs on a patch made of crosslinked monolayer gelatin nanofibers, J. Mater. Chem. B, 4 (2016) 3305-3312.

[35] Tang, Y.; Liu, L.; Li, J.; Yu, L.; Wang, L.; Shi, J.; Chen, Y. Induction and differentiation of human induced pluripotent stem cells into functional cardiomyocytes on a compartmented monolayer of gelatin nanofibers, Nanoscale, 8 (2016) 14530-14540.
[36] F. Gobeaux, G. Mosser, A. Anglo, P. Panine, P. Davidson, M.-M. Giraud-Guille, E. Belamie, J. Mol. Biol. 376 (2008) 1509-1522.
[37] M.-M. Giraud-Guille, L. Besseau, D. Herbage, P. Gounon, Optimization of Collagen Liquid Crystalline Assemblies: Influence of Sonic Fragmentation, J. Struct. Biol. 113 (1994) 99-106.
[38] I. Bergman, R. Loxley, Two Improved and Simplified Methods for the Spectrophotometric Determination of Hydroxyproline, Anal. Chem. 35 (1963) 1961-1965.
[39] C. Teulon, A. Tidu, F. Portier, G. Mosser, M.-C. Schanne-Klein, Probing the 3D structure of cornea-like collagen liquid crystals with polarization-resolved SHG microscopy, Opt. Express 24 (2016) 16084-16098.
[40] J. Schindelin, I. Arganda-Carreras, E. Frise, V. Kaynig, M. Longair, T. Pietzsch, S. Preibisch, C. Rueden, S. Saalfeld, B. Schmid, J.-Y. Tinevez, D.J. White, V. Hartenstein, K. Eliceiri, P. Tomancak, A. Cardona, Fiji: an open-source platform for biological-image analysis, Nature Methods, 9 (2012) 676-682.
[41] Z. Pincus, J.A. Theriot, Comparison of quantitative methods for cell-shape analysis, J. Microscopy, 227 (2007) 140-156.
[42] A. Lambert, A. Vanhecke, A. Archetti, S. Holden, F. Schaber, Z. Pincus, M.T. Laub, E. Goley, S. Manley, Constriction Rate Modulation Can Drive Cell Size Control and Homeostasis in C. crescentus, iScience, 4 (2018) 180-189.
[43] S.C. Wei, L. Fattet, J.H. Tsai, Y. Guo, V.H. Pai, H.E. Majeski, A.C. Chen, R.L. Sah, S.S. Taylor, A.J. Engler, J. Yang, Matrix stiffness drives epithelial-mesenchymal transition and tumour metastasis through a TWIST1-G3BP2 mechanotransduction pathway, Nat. Cell Biol., 17 (2015), 678.
[44] A.J. Rice, E. Cortes, D. Lachowski, B.C.H. Cheung, S.A. Karim, J.P. Morton, A. Del Río Hernández, Matrix stiffness induces epithelial-mesenchymal transition and promotes chemoresistance in pancreatic cancer cells, Oncogenesis, 6.7 (2017): e352-e352.
[45] B.F. Matte, A. Kumar, J.K. Placone, V.G. Zanella, M.D. Martins, A.J. Engler, M.L. Lamers, Matrix stiffness mechanically conditions EMT and migratory behavior of oral squamous cell carcinoma, J. Cell Sci., 132 (2019) jcs224360.
[46] Y. Dong, Q. Zheng, Z. Wang, X. Lin, Y. You, S. Wu, Y. Wang, C. Hu, X. Xie, J. Chen, D. Gao, Y. Zhao, W. Wu, Y. Liu, Z. Ren, R. Chen, J. Cui, Higher matrix stiffness as an independent initiator triggers epithelial-mesenchymal transition and facilitates HCC metastasis, J. Hematol. Oncol., 12 (2019) 112.
[47] M. Millet, R. Ben Messaoud, C. Luthold, F. Bordeleau, Coupling Microfluidic Platforms, Microfabrication, and Tissue Engineered Scaffolds to Investigate Tumor Cells Mechanobiology, Micromachines, 10 (2019) 418.
[48] W.J. Polacheck, A.E. German, A. Mammoto, D.E. Ingber, R.D. Kamm, Mechanotransduction of fluid stresses governs 3D cell migration, Proc. Natl. Acad. Sci. U S A, 111 (2014) 2447-52.
[49] F. Kai, A.P. Drain, V.M. Weaver, The Extracellular Matrix Modulates the Metastatic Journey, Dev. Cell. 49 (2019) 332-346.
[50] W.J. Polacheck, J.L. Charest, R.D. Kamm, Interstitial flow influences direction of tumor cell migration through competing mechanisms, Proc. Natl. Acad. Sci. U S A, 108 (2011) 11115-20.
[51] S. Nath, M. Pigula, A.P. Khan, W. Hanna, M.K. Ruhi, F.M. Dehkordy, K. Pushpavanam, K. Rege, K. Moore, Y. Tsujita, C. Conrad, F. Inci, M.G.D. Carmen, W. Franco, J.P. Celli, U. Demirci, T. Hasan, H.C. Huang, I. Rizvi, Flow-induced Shear Stress Confers Resistance to Carboplatin in an Adherent Three-Dimensional Model for Ovarian Cancer: A Role for EGFR-Targeted Photoimmunotherapy Informed by Physical Stress, J Clin Med. 9 (2020) 924.